



Dynamic stall simulation of a pitching airfoil under unsteady freestream velocity



Kobra Gharali, David A. Johnson*

Wind Energy Group, Department of Mechanical and Mechatronics Engineering, University of Waterloo, Waterloo, Canada N2L 3G1

ARTICLE INFO

Article history:

Received 22 May 2012

Accepted 6 May 2013

Available online 27 July 2013

Keywords:

Unsteady freestream velocity

Oscillating airfoil

Dynamic stall

SST $k-\omega$ model

Leading edge vortex

Trailing edge vortex

ABSTRACT

Effects of horizontal oscillations of the freestream velocity superimposed on a pitch oscillating NACA0012 airfoil were investigated using Computational Fluid Dynamics (CFD). The SST $k-\omega$ model coupled with a low-Reynolds number correction was applied for $Re \approx 10^5$, when the airfoil was undergoing dynamic stall. The main parameter ϕ , the phase difference between the freestream oscillation and the airfoil oscillation, was varied from 0 to π . The ϕ variation resulted in several times amplitude dynamic loads when $\phi \leq \pi/2$ to several times damping dynamic loads for $\phi > \pi/2$ where some dynamic stall loads were damped even below static stall load values. It was found that ϕ variation was divided into two main ranges based on the values of the unsteady freestream velocity at dynamic stall. The load variation also appeared with some differences including the shape of the trailing edge vortex sheet before stall, the circulation of the dynamic stall vortex pairs, the critical angles, vortex growth time and the secondary lift peak location that are discussed in detail.

© 2013 Elsevier Ltd. All rights reserved.

1. Introduction

Studying unsteady airloads on airfoils is important due to significant load variations particularly with dynamic stall events. Dynamic stall occurs when unsteady angle of attack (AOA) motion delays stall. This phenomena are associated with Leading Edge Vortex (LEV) formation. As the low pressure LEV grows, lift and drag coefficients rise until the stall point and then they drop dramatically. Because of this significant load variation, understanding dynamic stall phenomena is critical for designing and controlling systems operating under these conditions. Dynamic stall phenomena associated with pitch oscillating airfoils have been considered for many years with a wide range of applications such as helicopter blade rotors, wind turbines and maneuverable wings. For more than two decades, McCroskey and his colleagues made tremendous efforts to investigate the details of the dynamic stall phenomena (Ko and McCroskey, 1997; Martin et al., 1974). McCroskey also published two excellent reviews related to this study (McCroskey, 1981, 1982). Although extensive recent experimental studies (Lee and Basu, 1998; Lee and Gerontakos, 2004; Raffel et al., 1995; Sadeghi and Mani, 2009) as well as numerical studies (Barakos and Drikakis, 2003; Ekaterinaris, 1995; Mellen et al., 2003; Sheng et al., 2008; Spetzos et al., 2005; Wang et al., 2010a) or a combination of them (Wernert et al., 1996) have been reported, dynamic stall issues have not been addressed completely.

A time-varying freestream velocity is one of the important parameters for unsteady aerodynamic loads. Theoretical and experimental studies have shown that the effects of a time-varying freestream velocity are more significant in the presence

* Corresponding author. Tel.: +1 519 888 4567; fax: +1 519 885 5862.

E-mail address: da3johns@uwaterloo.ca (D.A. Johnson).

of separated and dynamic stalled flows. [Saxena et al. \(1977\)](#) conducted experimental studies to see the effects of the unsteady freestream and that group continued the work to show the dependency of the dynamic stall phenomena on the amplitude and frequency of periodic oscillations ([Hajek and Fejer, 1978](#); [Saxena et al., 1978](#)). [Pierce et al. \(1978\)](#) and [Kottapalli and Pierce \(1979\)](#) conducted experiments to demonstrate the effects of the accelerating and decelerating unsteady freestream during pitch oscillation of the airfoil when the frequency of the airfoil pitching was different from that of the freestream. The results of their work showed significant impacts on dynamic stall events. [Favier et al. \(1982, 1988\)](#) used fore-and-aft translational motion of the airfoil in a steady freestream to simulate relative instantaneous velocity variation. Based on their results, the phase difference between the unsteady velocity and the periodic AOA changed the magnitude and behavior of the aerodynamic loads significantly. That group continued the work using laser based techniques ([Berton et al., 2001](#)) and CFD modeling ([Favier, 2010](#); [Martinat et al., 2009](#)). Most of the above studies are based on the aerodynamics of helicopter rotors. In very recent studies, experiments were reported ([Shi and Ming, 2008, 2009](#)) with pitching delta wings under an unsteady freestream velocity with application to a maneuverable delta wing. The results showed that a decelerating freestream velocity during pitch up can delay the dynamic stall angle. Another application of this study is the unsteady incident velocity over the airfoils of a horizontal axis wind turbine. As mentioned before, in some of the previous studies, instead of an oscillating freestream, the equivalent movement of the body in a steady flow was studied. Recently, [Wong et al. \(2012, 2013\)](#) compared these two cases for a flat plate at a low reduced frequency. They showed that the non-circulatory (added-mass) term caused lift differences. Since the acceleration effects cannot be ignored, these two cases gave different results. Moreover, they indicated the added-mass term was not the only reason for the discrepancy between these two cases. Based on their findings the oscillating freestream and the oscillating body are not equivalent; thus, in the rest of this study, an unsteady freestream means an oscillating freestream. Because of the difficulties of creating a time-varying freestream experimentally, the problem of a time-varying freestream velocity is usually ignored. Thus, the usefulness of Computational Fluid Dynamic (CFD) approaches for evaluating this problem is apparent ([Leishman, 2006](#)).

Several published papers that are associated with the numerical simulation of a pitching NACA0012 airfoil are reported by [Amiralaei et al. \(2010\)](#) and [Lu et al. \(2013a\)](#) for laminar flows and by [Spentzos et al. \(2005\)](#), [Wang et al. \(2010a\)](#) and [Lu et al. \(2013b\)](#) for laminar to turbulent transition $Re \approx 10^5$ (with deep dynamic stall) where

$$Re = \rho c U_\infty / \mu, \quad (1)$$

and ρ and μ are the fluid density and viscosity respectively, c is the airfoil chord and U_∞ is the mean freestream velocity. All of these studies have been conducted based on a uniform freestream. To the authors' knowledge, no CFD simulation has been completed thus far to investigate the interaction of a pitch oscillating airfoil with an unsteady freestream velocity with the same oscillation frequency and high amplitude at $Re \approx 10^5$ which is the objective of this paper.

2. Specifications of simulated cases

A NACA0012 airfoil was pitch oscillating about the $\frac{1}{4}$ chord location according to the sinusoidal mode

$$\alpha = \alpha_{\text{mean}} + \alpha_{\text{amp}} \sin(2\pi ft), \quad (2)$$

where α_{mean} , α_{amp} and f represent mean AOA, pitch oscillation amplitude and oscillation frequency, respectively.

For the sinusoidally varying freestream, the horizontal velocity was oscillating governed by

$$\frac{U(t)}{U_\infty} = 1 + \lambda \sin(2\pi ft + \phi), \quad (3)$$

where λ is the reduced amplitude defined as

$$\lambda = \frac{U_{\text{amp}}}{U_\infty}, \quad (4)$$

and U_∞ of the steady freestream is considered as U_{mean} and ϕ represents the phase difference between the oscillation of the airfoil and the oscillation of the freestream velocity. The oscillation systems have the reduced frequency k , where

$$k = \frac{\pi f c}{U_\infty}. \quad (5)$$

The details of the cases in this study are provided in [Table 1](#). It should be noted that because of the availability of experimental results for a pitch oscillating, steady freestream condition ([Lee and Gerontakos, 2004](#)) to validate the CFD results, the pitch oscillating parameters are consistent for all cases.

3. Numerical set-up

3.1. Solver and turbulence model

The CFD flow solver package ANSYS Fluent 12.1 ([Fluent, 2009](#)) was employed to model the flow field over an oscillating airfoil under a constant freestream velocity as well as an unsteady freestream velocity. All simulations were run over 8 CPUs

Table 1

Details of simulated cases; values of all the parameters except those of freestream velocity oscillation are the same for both the numerical and the experimental setups (Lee and Gerontakos, 2004).

Airfoil	NACA0012
Reynolds number, Re	1.35×10^5
Inlet turbulent intensity	0.08%
Angle of attack oscillation (Eqs. (2) and (5))	
Reduced frequency, k	0.1
Mean angle of attack, α_{mean}	10°
Amplitude of oscillation, α_{amp}	15°
Freestream velocity oscillation (Eqs. (3) and (5))	
Reduced frequency, k	0.1
Reduced amplitude, λ	0.4, 0.6, 0.8
Phase difference of oscillations, ϕ	$0, \frac{\pi}{4}, \frac{\pi}{2}, \frac{3\pi}{4}, \pi$

in parallel using the facilities of the Shared Hierarchical Academic Research Computing Network (SHARCNET) and Compute/Calcul Canada.

In Fluent, Unsteady Reynolds Averaged Navier-Stokes (URANS) equations are solved based on the finite volume method. For the turbulence closure, the SST $k-\omega$ model (Menter, 1994), the combined model of the $k-\omega$ model and the $k-\epsilon$ model, was chosen. The SST $k-\omega$ model is capable of capturing the flow structures of dynamic airfoils associated with leading edge vortex formations for a wide range of Reynolds numbers (Ahmadi et al., 2009; Ol et al., 2009; Rival et al., 2011) with an acceptable accuracy. Although this model is for fully turbulent flow, it accommodates the transitional regime with a low-Reynolds number correction. With this correction, the turbulent viscosity (μ_t) is damped by the coefficient α^* (Fluent, 2009; Wilcox, 1998)

$$\alpha^* = \frac{0.024 + \frac{Re_t}{6}}{1 + \frac{Re_t}{6}}, \quad (6)$$

where

$$Re_t = \frac{\rho k}{\mu \omega}, \quad (7)$$

and k and ω are related to the $k-\omega$ model in this equation only.

3.2. Grid

A C-grid layout, Fig. 1, has been generated with ICEM CFD 12.1 (Fluent, 2009). The independence of the results from the grid resolution was examined with different grid sizes. The final grid utilized 2×10^5 cells, with 500 nodes around the airfoil while the location of the first row of cells kept $Y^+ < 1$. The locations of the boundaries are fixed at $20c$ from the airfoil, Fig. 2. More information related to the quality of the mesh is provided in Section 4.

3.3. Solver set-up

The airfoil and the whole computational domain was oscillating together according to Eq. (2) like a rigid body about the 1/4 chord location by a compiled user-defined function. Besides the dynamic mesh, the velocity of the freestream can oscillate horizontally described by Eq. (3) via a user-defined function to create an unsteady airstream, as shown in Fig. 2. At different angles, the straight sides of the domain can be either inlet or outlet. Since the boundary conditions were changing during pitching, inlet/outlet velocity was used for all external boundary conditions. The inlet/outlet velocity can be used if the overall continuity of the domain is fulfilled (Fluent, 2009) and the boundaries are far from the object. In this study, the inlet and outlet areas normal to the inflow velocity were always equal and the boundaries were located far enough from the object at $20c$. The inlet turbulence intensity of 0.08% reported for the experimental work by Lee and Gerontakos (2004) was very low compared to common wind tunnels, but for consistency, the same value was used for the numerical simulation. Since the flow is incompressible, the pressure based Navier Stokes solution algorithm was selected and for the pressure-velocity coupling scheme, the PISO algorithm was chosen. The second order upwind method for spatial discretization gave satisfactory results. The convergence criteria for the residuals were $\mathcal{O}(5 \times 10^{-5})$ in magnitude. As another criterion for judging the convergence, load values were monitored manually for the first few steps. After the loads and the other residuals converged, a small time step size was introduced for the rest of the simulation to ensure that the rest of the steps were converged. Moreover, to determine the optimum time step, a few simulations were run with shorter time steps and

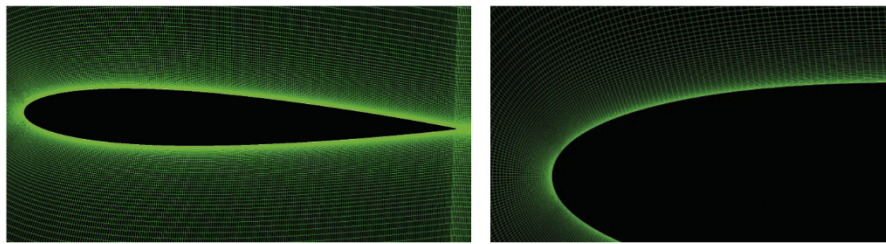


Fig. 1. C-type mesh around NACA0012 airfoil.

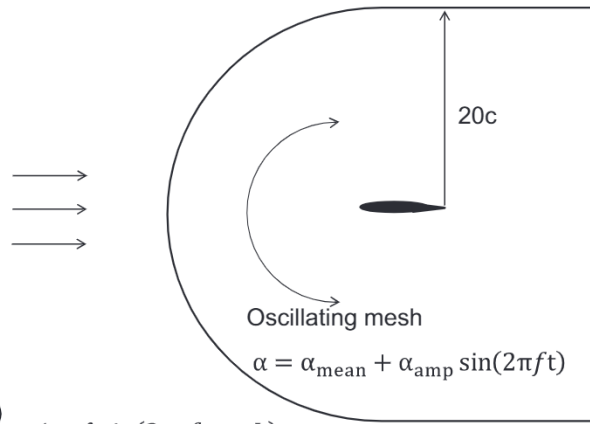


Fig. 2. Dynamic mesh facing horizontally unsteady freestream velocity.

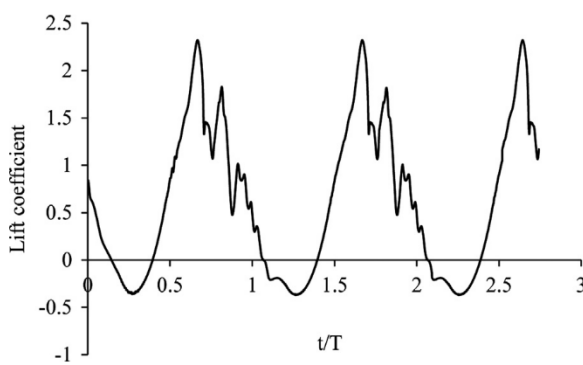


Fig. 3. History of the lift coefficient for the pitch oscillating airfoil.

the final resultant load loops were compared. When the load loops were temporally independent or were not changed by decreasing the time step, the optimum time step was obtained. The time step is usually presented based on the characteristic time of the airfoil, $dt = \tau(c/U_\infty)$. For the current study, the optimum τ was found to be 10^{-2} for all cases. Because a dynamic mesh was used, a first-order temporal discretization was fixed for the transient formulation by the software. After the first pitching cycle, shown in Fig. 3, the aerodynamic load loops become periodic even for the unsteady freestream velocity cases.

4. Numerical simulation validation

To confirm the accuracy of the numerical simulation, the instantaneous loads are compared with the existing experimental results of Lee and Gerontakos (2004) for sinusoidal pitch oscillation with a steady freestream in Fig. 4. This case was also numerically modeled by Wang et al. (2010a). They applied the same turbulence model, the SST $k-\omega$ model with low-Reynolds correction, but the aerodynamic loads showed an unstable behavior particularly during upstroke, as seen in the results of Wang et al. (2010a) shown in Fig. 5. It was found in this study that one of the key parameters to give a more

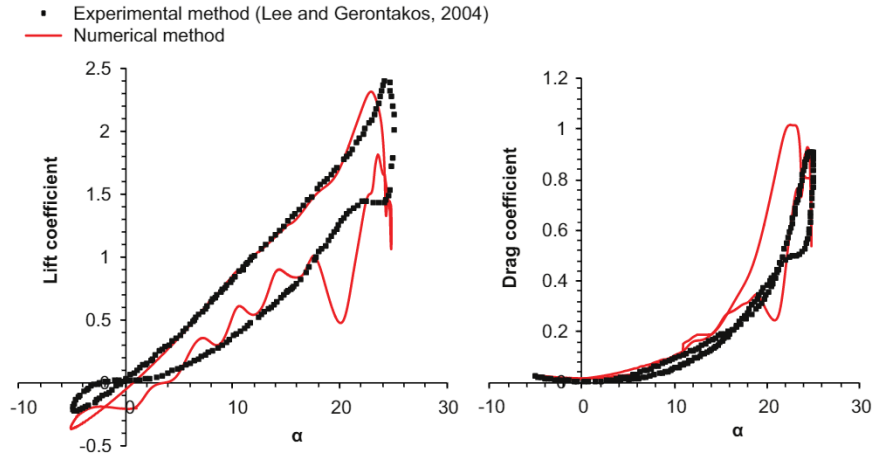


Fig. 4. Comparison of dynamic load loops from current numerical simulation and experimental method; Legend: ■ experimental data (Lee and Gerontakos, 2004), – simulation.

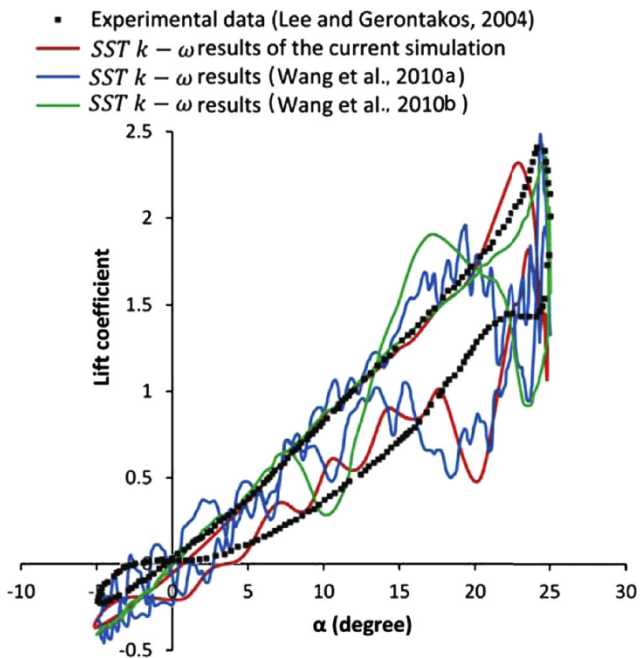


Fig. 5. Dynamic lift loops; comparisons of numerical simulations.

stable simulation is the cell skew factor. For the current mesh, the cell equi-angle skew is almost zero except for two small areas close to the leading and trailing edges with the maximum value of 0.1. If the value of this factor increases, the results become more unstable. Although the cell skew factor is always important for a quality mesh (Fluent, 2009), sometimes a much higher value can give good results for different cases, but for dynamic stall phenomena, this factor should be as small as possible. Wang et al. (2010b) in another study improved the results which are shown and compared with the current result also in Fig. 5. At pitch down motion, the current lift loop slightly oscillates around the experimental lift curve and it is closer to the experimental one than that of Wang et al. (2010b) which covers the upstroke curve instead of the downstroke one. These small oscillations during downstroke are a result of reattachment and relaminarization and are not related to the mesh quality.

Besides integral lift and drag forces, the wake streamwise velocity profiles from numerical and experimental methods are compared in Fig. 6. The numerical model predicts a narrower wake and smaller wake deficit. At $\alpha = 15^\circ \uparrow$ (upstroke), the flow is attached with a narrow wake. In this region there is a good agreement between the two methods. At higher AOA with separated flow, the wake deficit and the wake thickness increase. The wake profile at $\alpha = 25^\circ$ demonstrates massive separation after stall. The overall trends of the curves for $y/c < -0.3$ differ. There will be a discussion later that the numerical

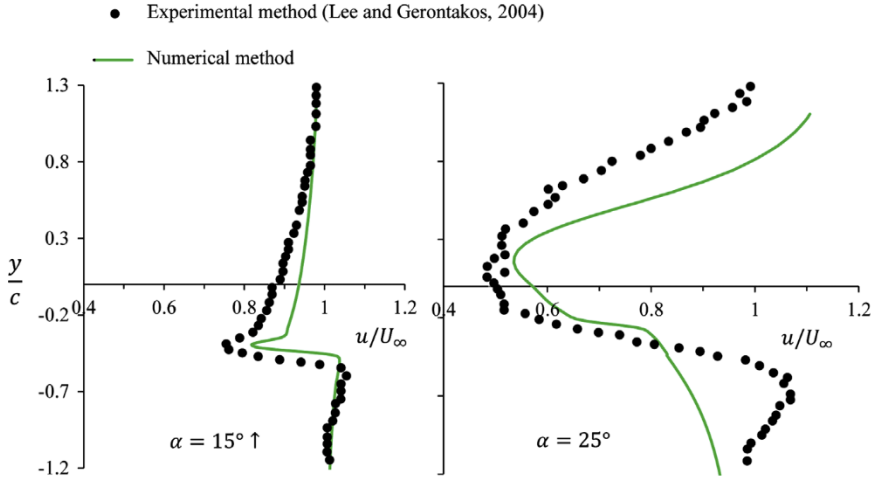


Fig. 6. Wake streamwise velocity profiles at one chord from the trailing edge of the airfoil.

simulation advances the dynamic stall point. Thus, the vortical structures as well as wake velocity profiles during post stall cannot be exactly the same for both methods.

5. Results and discussion

5.1. Pitching AOA with in-phase freestream velocity oscillation

For this case, the airfoil is sinusoidally pitch oscillating with

$$\alpha = 10 + 15 \sin(2\pi ft) \quad [\text{deg}], \quad (8)$$

while a time-varying freestream velocity,

$$\frac{U(t)}{U_\infty} = 1 + 0.6 \sin(2\pi ft) \quad (9)$$

is superimposed. The rest of the information can be found in [Table 1](#). For this case, when the AOA increases, the freestream velocity accelerates and in the same manner, at pitch down motion, the time varying freestream velocity decelerates. To see the dynamic effects of in-phase movement ($\phi = 0$), all the results for this case are compared with the pitch oscillating case with a steady freestream condition.

5.1.1. Aerodynamic loads

[Fig. 7](#) shows the aerodynamic loads for a pitch cycle for both a steady and unsteady freestream velocity. The aerodynamic loads based on unit span are normalized with the mean freestream velocity

$$[c_l, c_d] = \frac{[l, d]}{\frac{1}{2}\rho U_\infty^2 c}, \quad (10)$$

where l and d are the lift and drag forces. The main interest in dynamic stall phenomena is the load augmentation compared to the static stall, which are summarized in [Table 2](#). At points A and A' (prime ('') indicates the unsteady freestream velocity case), the reversed flow at the trailing edge moves upstream. For the steady freestream velocity, the aerodynamic coefficients are increased slightly compared to the static stall case. At this point, for the steady freestream velocity, the values from experimental and numerical results are very close showing that at upstroke the curves overlap as shown in [Fig. 4](#). For the unsteady freestream velocity, the lift coefficient is slightly higher at point A' . The lift coefficient increases with a constant slope until a Leading Edge Vortex (LEV) forms. The growing LEV increases the slope of the lift curves at point B and B' . Compared to the experimental results, the numerical simulation for the steady freestream velocity advances the stall point around 1.5° . The maximum lift value is underpredicted by less than 4.5% showing this numerical simulation can predict dynamic stall with good accuracy. The in-phase unsteady freestream velocity advances the stall point (point C') about 1.2° with an increase in more than 2.68 lift coefficient units compared with point C . Drag coefficients start to rise dramatically after points A and A' . Compared to the static stall, drag increases for points C and C' are 0.96 and 2.12 units for steady and unsteady freestream, respectively, showing the high impact of dynamic cases on the drag coefficients. After static stall (point SS), the drag coefficient increases, but after dynamic stall the drag coefficient drops significantly similar to the lift coefficient. There is a discrepancy between steady and unsteady freestream velocity during post stall. For the unsteady freestream, after point C' , another peak in aerodynamic loads is visible representing a very energetic leading edge vortex.

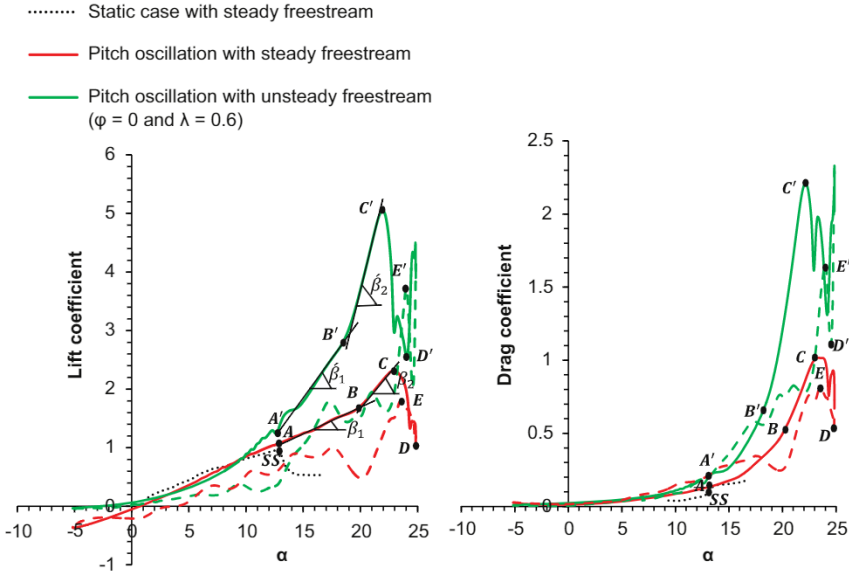


Fig. 7. Instantaneous loads. (A, A') flow reversal, (B, B') LEV, (C, C') stall point, (C–D, C'–D') full stall, (E, E') maximum downstroke peak, and (SS) static stall. Solid lines: upstroke, and broken lines: downstroke. ' indicates the unsteady freestream case.

Table 2
Summary of load augmentation—Pitching AOA.

	Steady freestream						Unsteady freestream				
	Experimental ^a			Numerical			Numerical ($\lambda = 0.6$ and $\phi = 0$)				
	α	ΔC_l^b	ΔC_d^c	Point	α	ΔC_l^b	ΔC_d^c	Point	α	ΔC_l^b	ΔC_d^c
Flow reversal	12.9°	0.12	0.00	A	12.9°	0.12	0.06	A'	12.9 °	0.50	0.13
LEV formation	21.9°	0.93	0.31	B	20.3°	0.85	0.46	B'	18.1°	1.77	0.58
First upstroke lift peak	24.7°	1.52	0.76	C	23.2°	1.40	0.96	C'	22.0°	4.08	2.12
First downstroke lift peak	21.8°	0.50	0.42	E	23.6°	0.95	0.75	E'	24.0°	2.80	1.60

^a Lee and Gerontakos (2004).

^b $\Delta C_l = C_l - C_l(\text{SS})$ where $C_l(\text{SS})$ is 0.92 (Lee and Gerontakos, 2004).

^c $\Delta C_d = C_d - C_d(\text{SS})$ where $C_d(\text{SS})$ is 0.0625 (Lee and Gerontakos, 2004).

More details are discussed in the next section. After points D and D', the first LEV at pitch down motion helps to recover part of the load coefficients leading to the first downstroke peak (Lee and Gerontakos, 2004; Leishman, 1990; Raffel et al., 1995; Wang et al., 2010a). The same scenario as the first upstroke maximum peak occurs for the first downstroke maximum peak; that means, point E is advanced compared to that of the experimental results and point E' occurs earlier than point E. Lift and drag values for point E' are 1.85 and 0.85 units higher than point E. For both steady and unsteady freestream velocities, the flows are fully attached close to $\alpha = -5^\circ$.

5.1.2. Flow structure

To interpret the behavior of the flow field under dynamic stall, the following figures have been prepared: Fig. 8 for the Turbulent Viscosity Ratio (TVR), Fig. 9 for the pressure coefficient and Fig. 10 for the non-dimensional vorticity field while Figs. 8 and 9 are superimposed with streamlines. In these figures, ↑ and ↓ indicate upstroke and downstroke, respectively. The TVR is defined as

$$\text{Turbulent Viscosity Ratio (TVR)} = \frac{\text{turbulent viscosity } (\mu_t)}{\text{molecular viscosity } (\mu)}, \quad (11)$$

and is an indicator of the flow turbulence behavior. If μ_t is greater than two orders of magnitude of μ , the flow can be considered as turbulent (Wang et al., 2010a). Based on the TVR field, Fig. 8, the flow is considered as turbulent when the TVR is close to 100.

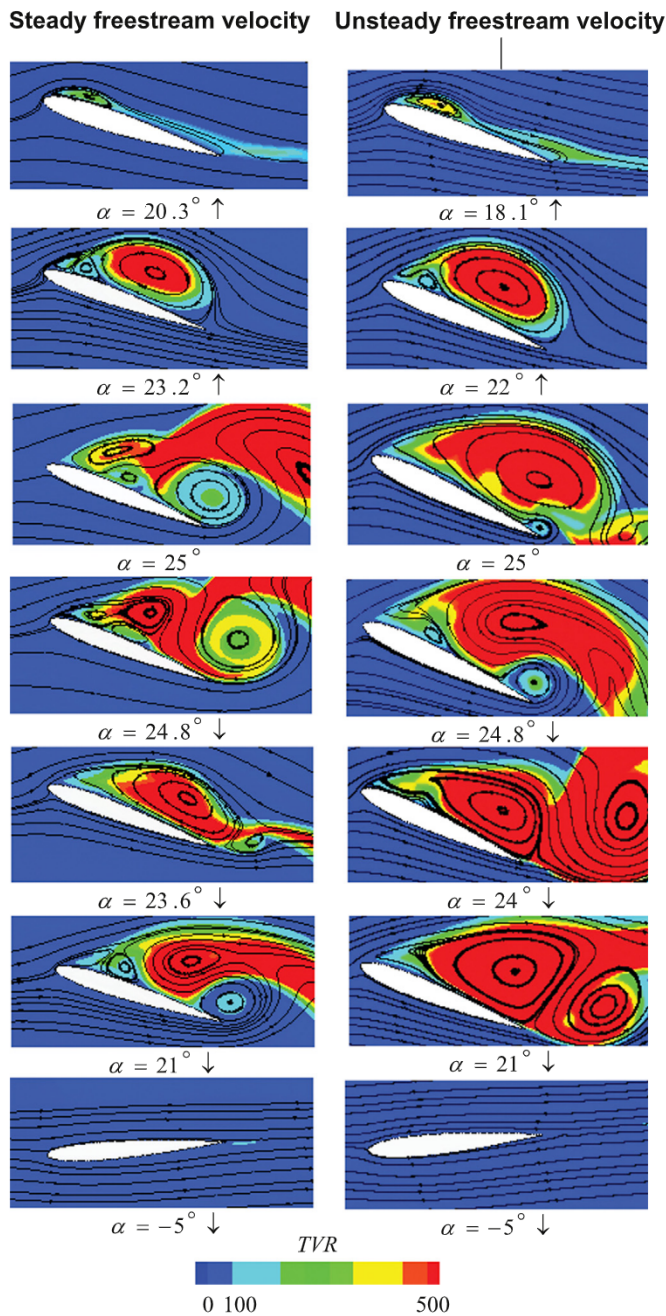


Fig. 8. Turbulent viscosity ratio field superimposed with flow streamlines for a pitching cycle with steady and unsteady freestream velocities ($\lambda = 0.6$ and $\phi = 0$ for unsteady freestream velocity).

Beginning with upstroke, the flow field undergoes different flow phenomena in a full cycle of pitch oscillation demonstrated in the following:

Attached flow and flow reversal: At very low AOA, laminar flow is attached to the airfoil surface except in the small trailing edge region which was also seen in experiments (Lee and Gerontakos, 2004). The reversed flow at the trailing edge for both steady and unsteady freestream velocities starts moving upstream at $\alpha = 12.9^\circ$. For the numerical simulation in Fig. 11, a superimposition of velocity vectors, vorticity field and streamlines indicates the existence of the reversed flow at the trailing edge ($\alpha = 16^\circ \uparrow$ for the steady freestream case). Reversed flow at the trailing edge was also reported in the experimental results (Lee and Gerontakos, 2004). According to the experimental results, another characteristic is a roughly linearly increasing lift coefficient (Lee and Gerontakos, 2004). Fig. 7 shows that the lift coefficient from the numerical simulation during $12.9^\circ < \alpha < 20.3^\circ$ has an almost constant slope β_1 . For the unsteady freestream case, a constant lift slope

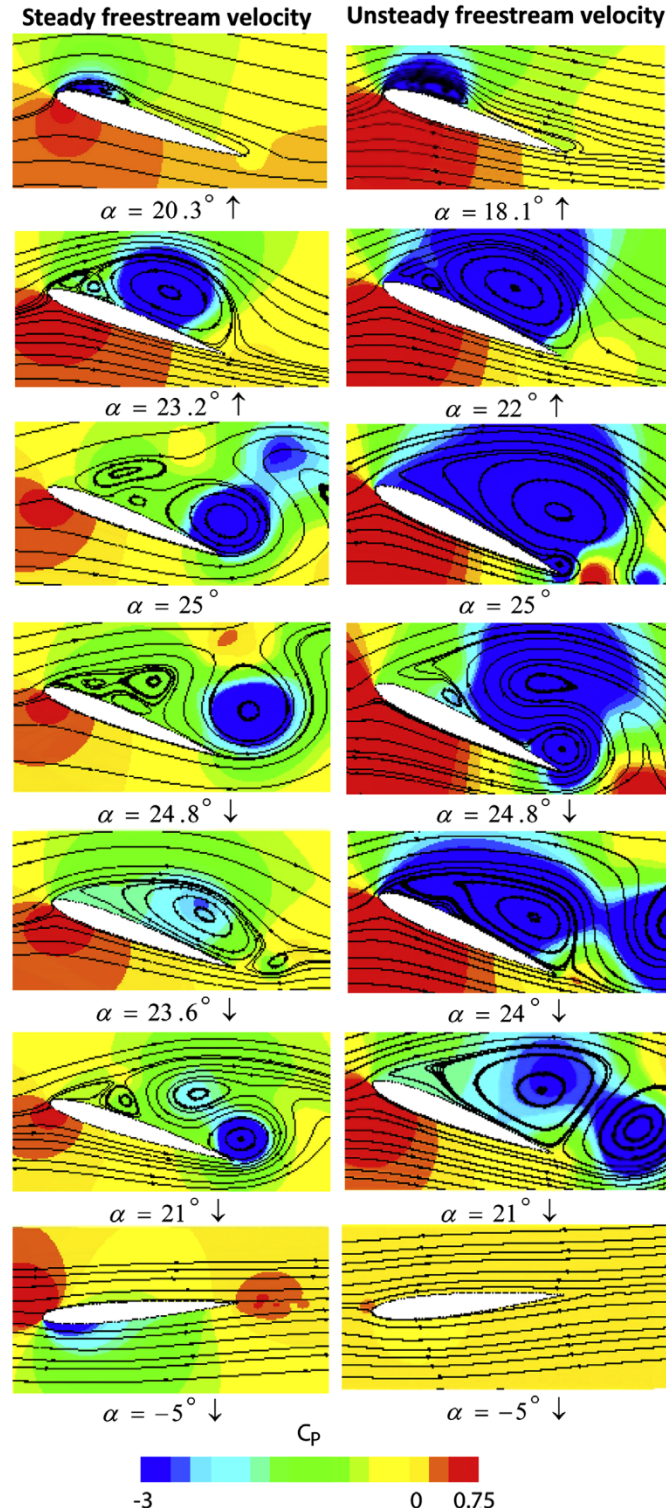


Fig. 9. Pressure coefficient superimposed with flow streamlines for a pitching cycle with steady and unsteady freestream velocities ($\lambda = 0.6$ and $\phi = 0$ for unsteady freestream velocity).

β'_1 during $12.9^\circ < \alpha < 18.1^\circ$ is also seen. For this case, the in-phase oscillating freestream is not changing the linear behavior of the lift augmentation, but the slope is much higher than that of the steady freestream case, $\beta'_1 > \beta_1$. Later in this section, there will be a discussion about the wake differences between these two cases.

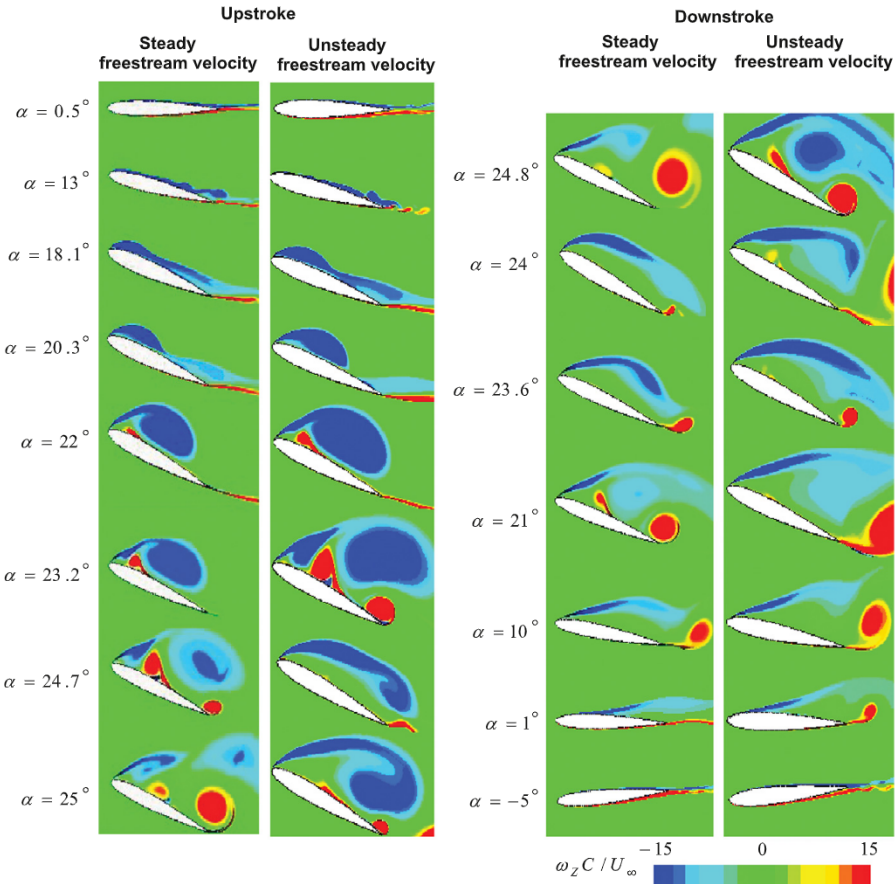


Fig. 10. Instantaneous vorticity field for a pitching cycle with steady and unsteady freestream velocities ($\lambda = 0.6$ and $\Phi = 0$ for unsteady freestream velocity).

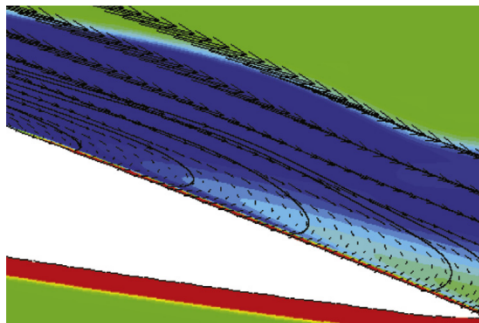


Fig. 11. Close up view of the flow reversal at $\alpha = 16^\circ \uparrow$ for the steady freestream case; the reversed flow visualized by velocity vectors and streamlines superimposed by the vorticity field which agrees with Lee and Gerontakos (2004), for legend see Fig. 10.

Leading edge vortex (LEV) formation: Later a LEV forms, grows and moves toward the trailing edge. Based on the experimental results (Lee and Gerontakos, 2004), LEV formation caused a sudden rise in aerodynamic loads. The same trend has been observed in the numerical loads (Fig. 7). The slopes of the lift curve change suddenly after $\alpha = 20.3^\circ$ (point B) and $\alpha = 18.1^\circ$ (point B') for steady and unsteady freestream velocities, respectively. LEV formations are shown in Figs. 8–10. For the steady freestream case, the LEV length is 28% of the chord length, twice the initial LEV length from experimental results. A LEV, a very low pressure vortex, enriches the strength of circulation resulting in an overshoot in the lift coefficient, shown in Fig. 7. For the unsteady freestream case, an accelerating freestream velocity results in the advancement of point B' by 2.2° compared to that of the steady freestream (point B) and increases the strength of the LEV causing higher aerodynamic loads before stall. After the LEV generation, the lift curve rises almost linearly with an increased slope $\beta_2 > \beta_1$ and $\beta'_2 > \beta'_1$ for steady freestream and unsteady freestream cases, respectively, while $\beta'_2 > \beta_2$ (Fig. 7).

Trailing edge vortex (TEV): The contributions of the first clockwise-rotating LEV, a source of circulation, to increase aerodynamic loads were discussed in detail. A counter-clockwise rotating vortex which is another source of circulation exists to satisfy conservation of circulation (Kelvin's circulation theorem). The difference in vortical structures can be visually enhanced if the vorticity fields are simply subtracted (Wong et al., 2013). Fig. 12 shows this instantaneous subtraction (ω_z , unsteady freestream case $- \omega_z$, steady freestream case). Before dynamic stall, the TEV mostly appears in vortex sheet form as shown in Fig. 12, for $\alpha = 10.5^\circ$ (before LEV formation), $\alpha = 18^\circ$ and $\alpha = 20.3^\circ$ (close to stall). After the airfoil passes the mean AOA (10°), where the velocities of the steady freestream and the unsteady freestream cases are the same, the difference between the aerodynamic loads between the two cases increases. At $\alpha = 10.5^\circ$, aerodynamic loads from the unsteady freestream case are slightly higher than those of the steady freestream. Although there is no sign of the LEV, the size of the TEV and the way that it is convected downstream can be one reason for the load difference. The TEV from the unsteady freestream appears as a longer vortex sheet. The longer vortex sheet from the unsteady freestream case follows Katz and Plotkin (2001) in that a longer vortex sheet of small vortices is favorable for a lift increase. At higher angles, the sheet of vortices are longer and their differences are more visible. Wong et al. (2012, 2013) also showed that the trailing edge vorticity variation affects the force history. For the unsteady freestream case, the velocity during upstroke is accelerating. By considering just the longitudinal freestream velocity after the mean AOA, the distance that a particle moves from the trailing edge under an unsteady freestream ($\int U(t)dt$) is more than that of the steady freestream ($U_{\text{mean}}\Delta t$). If the particles travel faster, the vortex sheet extends further to form a longer vortex sheet. The longer vortex sheet reduces the lift reduction caused by the TEV.

Secondary LEV formation: During the first LEV growth, a counter-clockwise vortex is generated close to the leading edge, shown at $\alpha = 22^\circ$ in Fig. 10. Beside it, a clockwise LEV is formed later to form a pair of LEV, shown at $\alpha = 23.2^\circ$. Gradually, the clockwise LEV is growing while the counter-clockwise one is moving rearward and disappearing. This complicated structure indicates an unstable boundary layer during the second LEV formation (Wang et al., 2010a).

Stall: As LEVs are growing, the first low pressure LEV occupies more of the suction surface area resulting in an increase of the normal force on the pressure surface. Dynamic stall occurs when the lift reaches its maximum value and based on the vorticity field, dynamic stall occurs when the outer surface of the LEV meets the trailing edge. Fig. 13 shows a close up view of the vortical field of dynamic stall overlaid with the streamlines for the unsteady freestream case. For all cases in this study, the outer surface of the LEV streamlines meets the trailing edge that is also seen in the vorticity field. Streamlines in Figs. 8 and 9 show the LEV for a steady freestream velocity at $\alpha = 23.2^\circ$ and for an unsteady freestream velocity at $\alpha = 22^\circ$. At this point the airfoil is stalled and a high TVR dominates the LEV as shown in Fig. 8. In Fig. 9, for the unsteady freestream velocity, very low pressure on the suction side and very high pressure on the pressure side compared to the steady freestream velocity indicates high loading on the airfoil.

LEV shedding: After stall, the LEV keeps growing in size and then leaves the suction surface. In Fig. 10, the first separated LEV in the wake is visible at $\alpha = 24.7^\circ$ and $\alpha = 23.2^\circ$ for steady and unsteady freestream velocities, respectively. During the

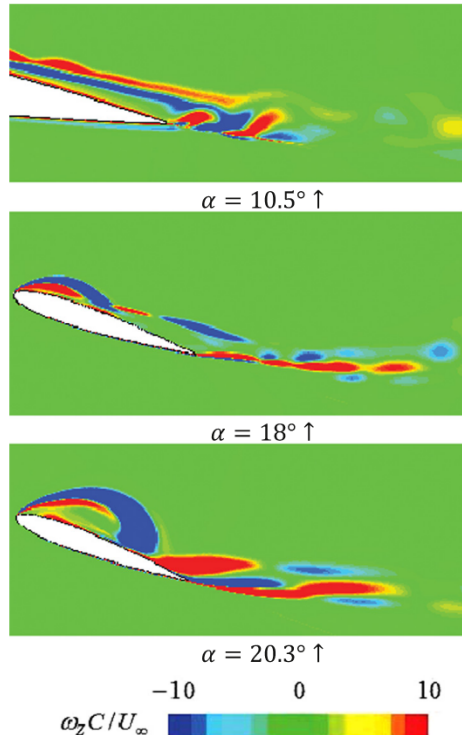


Fig. 12. Instantaneous vorticity field subtraction between the unsteady freestream ($\lambda = 0.6$ and $\phi = 0$) and steady freestream cases before dynamic stall.

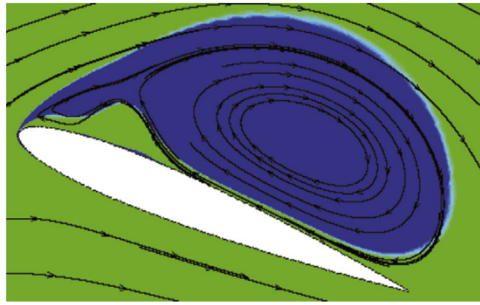


Fig. 13. Close up view of the dynamic stall vorticity field (negative values) covered with streamlines for the in-phase unsteady freestream case; for legend see Fig. 10.

shedding process, a large area on the suction surface has high TVR values especially for the unsteady freestream case seen in Fig. 8.

Full stall TEV: After dynamic stall, the counter-clockwise vortex gradually rolls up and finally sheds to the wake. Fig. 10 shows the growing and shedding of the first negative roll up vortex after $\alpha = 23.2^\circ \uparrow$ to $\alpha = 24.8^\circ \downarrow$ for a steady freestream velocity. For an unsteady freestream velocity, the process of formation to shedding of the first TEV occurs in 2° , after $\alpha = 22^\circ \uparrow$ to $\alpha = 24^\circ \downarrow$. The developed TEV has a TVR value (Fig. 8) greater than 100, a very low static pressure level (Fig. 9) and high vorticity magnitude (Fig. 10). The TEV has been shed to the wake before the next LEV covers the whole suction surface and then the next TEV is initialized.

Secondary upstroke LEV growth and shedding: The boundary layer of the unsteady freestream case feeds a secondary LEV with high vorticity. Therefore, this very low pressure secondary LEV grows in size rapidly and then creates the second load peak at $\alpha = 24.7^\circ \uparrow$ where this secondary LEV covers the whole suction surface, shown in Fig. 10, and then it is shed to the wake, $\alpha = 25^\circ$ in Fig. 10. For the steady freestream velocity, the secondary LEV is shed at downstroke. For the rest of the cases, the location of the second maximum lift peak related to the secondary LEV will be discussed in Sections 5.2 and 5.3.

First downstroke LEV growth and shedding: Gradually, at downstroke, the negative vortex of the leading edge vortex pair occupies the suction surface. Similar to the first LEV, increasing the size of the vortex recovers the lift force to create a maximum peak in downstroke. For the steady freestream velocity, at $\alpha = 23.6^\circ \downarrow$, the vortex reaches the trailing edge and then starts to shed. For the unsteady freestream velocity, the maximum lift occurs at $\alpha = 24^\circ \downarrow$. Figs. 7 and 10 show that the first downstroke LEV is not as strong as the upstroke one and that the aerodynamic coefficients do not recover to the values at the stall point.

Small vortices: Fig. 7 shows small lift peaks after the first downstroke LEV for both steady and unsteady freestream velocities. These are the result of small vortices which have very low circulation. Fig. 10 shows some of these small vortices after $\alpha = 23.6^\circ \downarrow$, and $\alpha = 24^\circ \downarrow$ for steady and unsteady freestream velocities.

Reattached flow: At $\alpha = 1^\circ \downarrow$ for both steady and unsteady freestream velocity, all small vortices have disappeared, but the flows are not fully attached at the trailing edge which agrees with the experimental results (Lee and Gerontakos, 2004).

5.1.3. Circulation and pinch-off process

Based on Stoke's theorem, the targeted vortex circulation, Γ , inside a rectangular area A can be calculated,

$$\Gamma = \iint_A \omega_z dA. \quad (12)$$

The clockwise vortex and counter-clockwise vortex are separated with a zero threshold value and considered for the LEV circulation, Γ_{LEV} , and the TEV circulation, Γ_{TEV} , respectively (Prangemeier et al., 2010).

Fig. 14 compares the dimensionless circulation for the first LEV and the following TEV for steady and unsteady freestream cases. For the unsteady freestream case, the circulation of the LEV has a greater slope and reaches the maximum value sooner in comparison to that of the steady case. The accelerating freestream speeds feeding of the LEV in the boundary layer. Dynamic stall is advanced for the unsteady freestream case about 1.2° compared to the steady freestream case while the circulation is 1.5 times greater. In Fig. 14, the phase delay ($\Delta\alpha$) shows that the maximum LEV circulation occurs later than the peak lift distribution (dynamic stall). Rival et al. (2010) found for their case study that there was a slight phase delay and the rolled-up TEV formation occurred right after the maximum LEV circulation. According to Fig. 14, this phase delay ($\Delta\alpha \approx 1.4^\circ$) cannot be ignored and the TEV is formed after dynamic stall. Fig. 15 shows the TEV clearly after dynamic stall and before peak circulation for the steady freestream case. This means that after dynamic stall, the boundary layer keeps feeding the LEV where $\Delta\Gamma_{LEV}/U_\infty c = 0.45$ and 0.7 for the steady and unsteady freestream cases, respectively and at the same time the TEV is growing and rolling up where $\Delta\Gamma_{TEV}/U_\infty c = 2$ and 2.8 for the steady and unsteady freestream cases, respectively. Since the TEV has a negative effect on lift augmentation, an increase in the TEV circulation contributes to the lift reduction despite the LEV growth. When the LEV pinches off, the boundary layer stops feeding it and this location is the maximum circulation. The overall trends of the TEV circulation curves are similar in Fig. 14. The TEV circulation curve for the steady freestream, compared to that of the unsteady freestream, is shifted due to the dynamic stall delay and has lower circulation

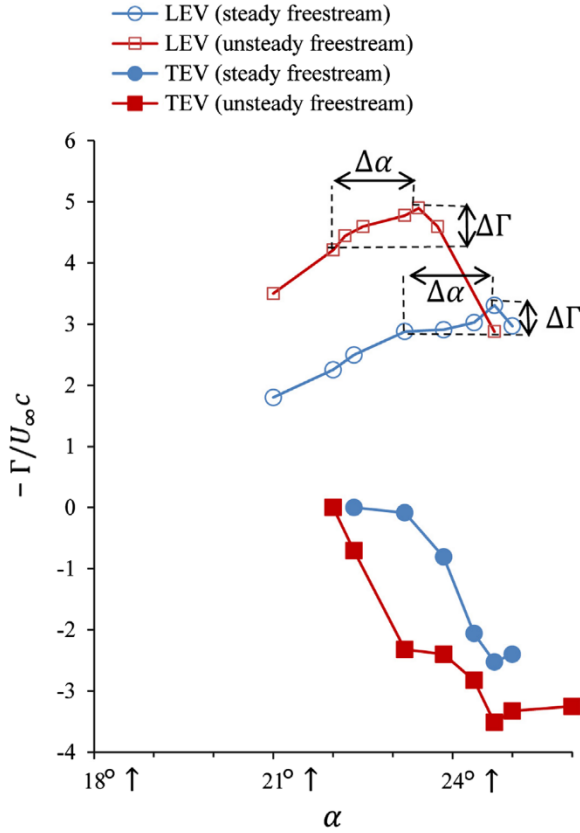


Fig. 14. LEV and TEV dimensionless circulation for the steady freestream and unsteady freestream cases ($\lambda = 0.6$ and $\phi = 0$). Lines are for visualization only. $\Delta\alpha$: Phase delay between the maximum lift (dynamic stall) and the maximum circulation.

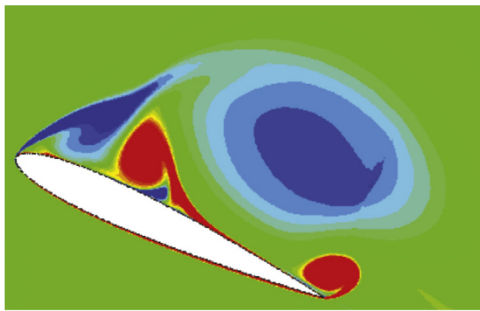
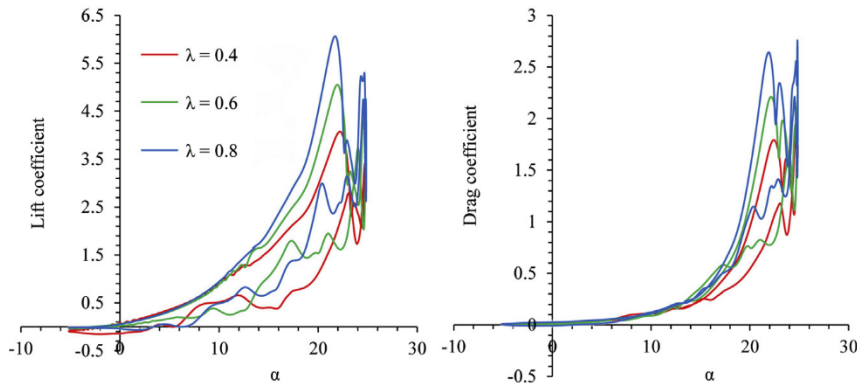


Fig. 15. TEV formation after dynamic stall and before LEV separation at $\alpha = 24.4^\circ \uparrow$ for steady freestream case; for legend see Fig. 10.

similar to the LEV circulation cases above. This indicates that the strengths of the LEV and the TEV are strongly connected which agrees well with the results of Prangemeier et al. (2010).

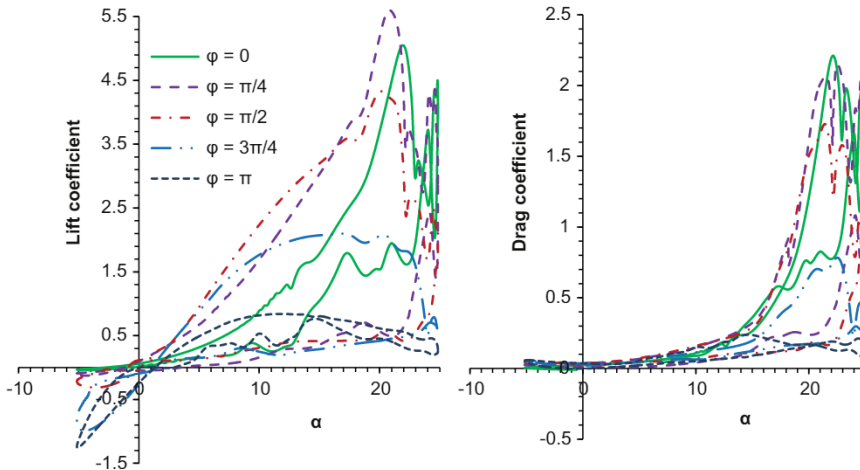
5.2. Reduced amplitude, λ , influences

Three different reduced amplitude ($\lambda = 0.4, 0.6$ and 0.8) cases were studied. For this section, $\phi = 0$ was chosen while the rest of the information is the same as in Table 1. A comparison of aerodynamic coefficients in Fig. 16 shows that increasing 0.2 units of λ advances the stall point slightly (Table 3) and increases the lift and drag coefficients almost 1 and 0.5 units, respectively, because the velocity of the freestream during dynamic stall is higher. Aerodynamic load enrichment with increasing λ has also been reported by Leishman (2002). At low angles of incidence, there is no significant difference. The overall form of the curves is almost the same for these cases and the secondary lift peak at upstroke from the secondary LEV exists for all three cases. The behavior of the boundary layer in advancing the secondary peak will be discussed in the next section.

Fig. 16. Aerodynamic loads for $\lambda = 0.4, 0.6$ and 0.8 with $\phi = 0$.**Table 3**

Summary of critical angles of attack.

Pitch oscillation with unsteady freestream		First upstroke lift peak	Second upstroke lift peak	First downstroke lift peak
λ	ϕ			
0.4	0	22.3°	24.8°	22.9°
0.6	0	22.0°	24.4°	24.0°
0.8	0	21.7°	24.0°	24.5°
0.6	$\pi/4$	21.0°	24.0°	24.1°
0.6	$\pi/2$	20.2°	24.3°	21.0°
0.6	$3\pi/4$	22.4°	—	24.0°
0.6	π	24.6°	—	20.3°

Fig. 17. Aerodynamic loads for $\phi = 0, \pi/4, \pi/2, 3\pi/4$ and π with $\lambda = 0.6$.

5.3. Phase difference of oscillation, ϕ , impacts

The effects of the phase difference between the oscillation of the airfoil and oscillation of the freestream velocity on aerodynamic loads are now considered. For this section, $\lambda = 0.6$ was chosen and the rest of the information is the same as in Table 1. Fig. 17 shows lift and drag coefficients for $\phi = 0, \pi/4, \pi/2, 3\pi/4$ and π . The results show the significant impact of the ϕ parameter on loads. For $\phi \leq \pi/2$, the loads are significantly high, the first maximum peak moves forward and the second LEV shedding occurs at upstroke. More details about the critical AOA are provided in Table 3. For $\phi > \pi/2$, the second LEV shedding is postponed to the downstroke (for $\phi = 3\pi/4$, it is completely at downstroke) which is similar to that of pure pitch oscillation and is consistent with the results of Favier et al. (1982) from their experimental facilities. For $\phi > \pi/2$, although separation of the first LEV is postponed, the LEV cannot increase the aerodynamic loads. For the $\phi = \pi$ case, the aerodynamic

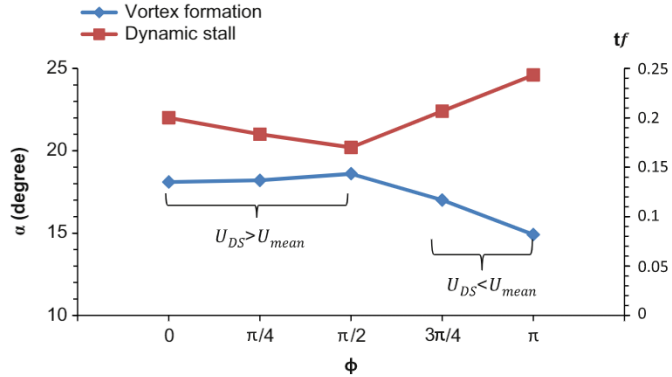


Fig. 18. The angles and times of LEV formation and dynamic stall versus ϕ during upstroke ($\lambda = 0.6$); time difference between two curves for each ϕ shows the vortex growth time; lines are for visualization purposes.

loads during the dynamic stall process ($\alpha > 15^\circ \uparrow$) are much smaller than those of the pitch oscillating case with uniform freestream velocity; that means, dynamic loads are damped significantly.

The behavior of the boundary layer based on vortex growth time from the LEV formation to dynamic stall is shown in Fig. 18 which reveals two different trends. In this figure, the time is made dimensionless by the frequency of the oscillations, f . The time difference between curves for each ϕ shows the vortex growth time. As ϕ increases from the zero value to $\phi = \pi/2$, the vortex growth time is decreasing continually, but for $\phi > \pi/2$, the trend is reversed and vortex growth time increases. Thus, the chart is divided in two regions. In the first region, as ϕ increases from the zero value, the maximum freestream velocity, U_{max} , shifts forward before the dynamic stall angle which affects the force history before stall while the freestream velocity during dynamic stall (DS), U_{DS} , is greater than U_{mean} . If dynamic stall occurs sooner, it becomes closer to U_{max} , which is suitable for load augmentation and then the vortex growth time is decreased. Moreover, in this region, all the secondary lift peaks occur during upstroke. For a pure pitch oscillating airfoil under a steady freestream, the second lift peak can be advanced to an upstroke location when the reduced frequency is decreased (McCroskey et al., 1976). Under low reduced frequency, the aerodynamic loads are decreased, but for the unsteady freestream case the loads are significantly increased when the second peak is located during upstroke $0 \leq \phi \leq \pi/2$. It is concluded that in the first region, the boundary layer does not follow the behavior of pitch oscillating airfoils as mentioned in McCroskey et al. (1976). For the second region, $\phi > \pi/2$, U_{DS} is lower than U_{mean} and U_{max} occurs away from dynamic stall at very low angles. In this range, the boundary layer delays dynamic stall to increase the loads. As a result, vortex growth time is increased. It should be mentioned that because U_{DS} is very slow, the overall load is very low in this range. In these two regions, the boundary layer behaves differently and then the previous assumption of increasing the vortex growth time for load augmentation cannot always be correct.

6. Conclusion

A pitch oscillating NACA0012 airfoil was simulated numerically to understand the problem of a lifting object under dynamic stall associated with unsteady freestream velocity at low Reynolds number, $Re \approx 10^5$. The cyclical forces and flow structures including LEV-TEV initiation, propagation and shedding agreed well qualitatively and quantitatively with those existing in the literature.

Increases in loads in the dynamic case are challenging from design and control points of view. From the results of this study, the aerodynamic loads show that for a pure pitch oscillating airfoil under a uniform freestream velocity, the stall point lift coefficient is 2.5 times greater than that of the static airfoil. The lift augmentation is more significant when the pitch oscillating airfoil is combined with an oscillating freestream with $0 \leq \phi \leq \pi/2$. The in-phase oscillations, $\phi = 0$, showed 5.4 times greater lift than that of the static freestream. This value was amplified when the reduced amplitude was increased. The low pressure LEV caused a very high pressure difference between the pressure surface and the suction surface when the flow was not attached indicating that very high loads are applied to the airfoil for the $\phi = 0$ case. As a future study, three dimensional modeling of the flow field will reveal more details of the dynamic stall phenomena. Comparing the steady and in-phase unsteady freestream cases showed that high LEV circulation was favorable for high lift values and the coupled strength of the LEV and TEV resulted in higher circulation for the TEV. Vortex circulation revealed a significant phase delay of LEV pinch-off (maximum circulation) after dynamic stall (maximum lift). During this phase lag, the TEV was growing, rolling up and decreased the lift values although the boundary layer was feeding the LEV. The contribution of the TEV to lift values was more visible when it appeared like a vortex sheet before dynamic stall. An accelerating freestream during dynamic stall speeds the vortex sheet expansion in the wake. The resultant longer vortex sheet for in-phase unsteady freestream increased lift significantly before stall since the longer trailing edge vortex sheet was favorable for increasing lift values.

The high phase difference, $\phi > \pi/2$, decreases the aerodynamic loads. For the $\phi = \pi$ case, the lift and drag loads are almost 3 and 5 times, respectively, lower than those of pitch oscillation with the steady freestream velocity case. The dynamic stall loads for this case were even lower than those of static stall which is opposite to the concept of dynamic stall which usually augments loads.

Despite variation in the loads, decreasing ϕ from $\phi = \pi/2$ and increasing ϕ from $\phi = \pi/2$ have an important common characteristic: they both increase the vortex growth time. This result reveals an important insight that increasing vortex growth time can either increase or decrease the dynamic stall loads since the location of the maximum freestream velocity affects the force history before stall.

Acknowledgements

The authors would like to acknowledge the support of the Natural Sciences and Engineering Research Council of Canada and Ontario Centers of Excellence, the facilities of the Shared Hierarchical Academic Research Computing Network (SHARCNET: www.sharcnet.ca) and Compute/Calcul Canada which made this work possible, Professor Daniel Favier from Aix-Marseille University, Institute of Movement Sciences, France, for sharing his deep knowledge in analyzing the results, and Shengyi Wang from the National Key Laboratory of Science and Technology on Aero-Engine Aero-thermodynamics, Beihang University, China for his advice on the numerical setup.

References

- Ahmadi, S.A., Sharif, S., Jamshidi, R., 2009. A numerical investigation on the dynamic stall of a wind turbine section using different turbulent models. *World Academy of Science, Engineering and Technology* 58, 290–296.
- Amiralaei, M.R., Alighanbari, H., Hashemi, S.M., 2010. An investigation into the effects of unsteady parameters on the aerodynamics of a low Reynolds number pitching airfoil. *Journal of Fluids and Structures* 26 (6), 979–993.
- Barakos, G., Drikakis, D., 2003. Computational study of unsteady turbulent flows around oscillating and ramping airfoil. *International Journal of Numerical Methods in Fluids* 42, 163–186.
- Bertot, E., Favier, D., NsiMba, M., Maresca, C., Allain, C., 2001. Embedded LDV measurement methods applied to unsteady flow investigation. *Experiments in Fluids* 30, 102–110.
- Ekaterinaris, J., 1995. Numerical investigation of dynamic stall of an oscillating wing. *AIAA Journal* 33, 1803–1808.
- Favier, D., 2010. The role of wind-tunnel experiments in CFD validation. *Encyclopedia of Aerospace Engineering* 1, 351–366.
- Favier, D., Agnes, A., Barbi, C., Maresca, C., 1988. The combined translation-pitch motion a new airfoil dynamic stall simulation. *Journal of Aircraft* 9, 805–814.
- Favier, D., Maresca, C., Rebont, J., 1982. Dynamic stall due to fluctuations of velocity and incidence. *AIAA Journal* 20, 865–871.
- Fluent, 2009. ANSYS Inc ANSYS FLUENT 12.1 (Theory Guide). URL <http://WWW.Fluent.com>.
- Hajek, T., Fejer, A., 1978. A new approach to rotor blade stall analysis. In: Fourth European Rotorcraft and Powered Lift Aircraft Forum, Stresa, Italy.
- Katz, J., Plotkin, A., 2001. Low Speed Aerodynamics. Cambridge University Press, Cambridge.
- Ko, S., McCroskey, W., 1997. Computations of unsteady separating flows over an oscillating airfoil. *AIAA Journal* 35, 1235–1238.
- Kottapalli, S.B.R., Pierce, G.A., 1979. Drag on an oscillating airfoil in a fluctuating free stream. *Journal of Fluids Engineering* 101, 391.
- Lee, T., Basu, S., 1998. Measurement of unsteady boundary layer developed on an oscillating airfoil using multiple hot-film sensors. *Experiments in Fluids* 25, 108–117.
- Lee, T., Gerontakos, P., 2004. Investigation of flow over an oscillating airfoil. *Journal of Fluid Mechanics* 512, 313–341.
- Leishman, J., 1990. Dynamic stall experiments on the NACA 23012 airfoil. *Experiments in Fluids* 9 (1), 49–58.
- Leishman, J.G., 2002. Challenges in modelling the unsteady aerodynamics of wind turbines. *Wind Energy* 5, 85–132.
- Leishman, J.G., 2006. Principles of Helicopter Aerodynamics. Cambridge Aerospace Series, vol. 18. Cambridge University Press, Cambridge.
- Lu, K., Xie, Y.H., Zhang, D., 2013a. Numerical study of large amplitude, nonsinusoidal motion and camber effects on pitching airfoil propulsion. *Journal of Fluids and Structures* 36, 184–194.
- Lu, K., Xie, Y.H., Zhang, D., Lan, J.B., 2013b. Numerical investigations into the asymmetric effects on the aerodynamic response of a pitching airfoil. *Journal of Fluids and Structures* 39, 76–86.
- Martin, J.M., Empey, R.W., McCroskey, W.J., Caradonna, F.X., 1974. An experimental analysis of dynamic stall on an oscillating airfoil. *Journal of the American Helicopter Society*, 26–32.
- Martinat, G., Braza, M., Harrana, G., Sevrain, A., Tzabiras, G., Hoarau, Y., Favier, D., 2009. Dynamic stall of a pitching and horizontally oscillating airfoil. In: IUTAM Symposium on Unsteady Separated Flows and their Control, vol. 14. Springer, Netherlands.
- McCroskey, W., 1981. The phenomenon of dynamic stall. Technical report, NASA TM-81264.
- McCroskey, W., 1982. Unsteady airfoils. Annual Review of Fluid Mechanics 14, 285–311.
- McCroskey, W.J., Carr, L.W., McAlister, K., 1976. Dynamic stall experiments on oscillating airfoils. *AIAA Journal* 14, 57–63.
- Mellen, C., Frohlich, J., Rodi, W., 2003. Lessons from LESFOIL project on large-eddy simulation of flow around an airfoil. *AIAA Journal* 41, 573–581.
- Menter, F.R., 1994. Two-equation eddy-viscosity turbulence models for engineering applications. *AIAA Journal* 32, 1598–1605.
- Ol, M.V., Bernal, L., Kang, C.K., Shyy, W., 2009. Shallow and deep dynamic stall for flapping low Reynolds number airfoils. *Experiments in Fluids* 46, 883–901.
- Pierce, G., Kunz, D., Malone, B., 1978. The effect of varying freestream velocity on dynamic stall characteristics. *Journal of the American Helicopter Society* 23, 27–33.
- Prangemeier, T., Rival, D., Tropea, C., 2010. The manipulation of trailing-edge vortices for an airfoil in plunging motion. *Journal of Fluids and Structures* 26 (2), 193–204.
- Raffel, M., Kompenhans, J., Wernert, P., 1995. Investigation of the unsteady flow velocity field above an airfoil pitching under deep dynamic stall conditions. *Experiments in Fluids* 19, 103–111.
- Rival, D., Hass, G., Tropea, C., 2011. The recovery of energy from leading- and trailing-edge vortices in tandem-airfoil configurations. *Journal of Aircraft* 48 (1), 203–211.
- Rival, D., Manejov, R., Tropea, C., 2010. Measurement of parallel blade-vortex interaction at low Reynolds numbers. *Experiments in Fluids* 49 (1), 89–99.
- Sadeghi, H., Mani, M., 2009. Measurements of the flow field behind a helicopter blade using the hot-wire anemometry. *Journal of Information Communication Technology* 2, 32–39.
- Saxena, L., Fejer, A., Morkovin, M., 1977. Features of unsteady flows over airfoils. In: Proceedings of the AGARD-FDP Meeting of Unsteady Aerodynamics, Ottawa, Ontario, Canada. pp. 22.1–22.11.

- Saxena, L., Fejer, A., Morkovin, M.V., 1978. Effects of periodic changes in freestream velocity on flows over airfoils near static stall. In: Nonsteady Fluid Dynamics: Proceedings of the Winter Annual Meeting, San Francisco, California.
- Sheng, W., Galbraith, R., Coton, F., 2008. A modified dynamic stall model for low Mach numbers. ASME Journal of Solar Energy Engineering 130, 310–313.
- Shi, Z.-W., Ming, X., 2008. Effects of unsteady freestream on aerodynamic characteristics of pitching delta wing. Journal of Aircraft 45, 2182–2185.
- Shi, Z.-W., Ming, X., 2009. Experimental investigation on a pitching motion delta wing in unsteady free stream. Modern Physics Letters B 23, 409–441.
- Spentzos, A., Barakos, G., Badcock, K., Richards, B., Wernert, P., Schreck, S., Raffel, M., 2005. Investigation of three-dimensional dynamic stall using computational fluid dynamics. AIAA Journal 43, 1023–1033.
- Wang, S., Ma, L., Ingham, D., Pourkashanian, M., Tao, Z., 2010a. Numerical investigations on dynamic stall of low Reynolds number flow around oscillating airfoils. Computers and Fluids 39, 1529–1541.
- Wang, S., Tao, Z., Ma, L., Ingham, D., Pourkashanian, M., 2010b. Numerical investigations on dynamic stall associated with low Reynolds number flows over airfoils. In: IEEE Second International Conference on Computer Engineering and Technology, vol. 5. pp. 308–312.
- Wernert, P., Geissler, W., Kompenhans, J., Raffel, M., 1996. Experimental and numerical investigations of dynamic stall on a pitching airfoil. AIAA Journal 34 (5), 982–989.
- Wilcox, D.C., 1998. Turbulence Modeling for CFD. DCW Industries, Inc., La Canada, California.
- Wong, J., Mohebbian, A., Kriegseis, J., Rival, D., 2012. On the simulation of complex gusts at low Reynolds numbers. In: 30th AIAA Applied Aerodynamics Conference, New Orleans, Louisiana.
- Wong, J., Mohebbian, A., Kriegseis, J., Rival, D., 2013. Rapid flow separation for transient inflow conditions versus accelerating bodies: an investigation into their equivalency. Journal of Fluids and Structures 40, 257–268.